Geometrical image distortion and aberration for long-range targets in a non-homogeneous atmosphere

Arie N. de Jong
TNO - Physics and Electronics Laboratory, The Hague – Netherlands

ABSTRACT

When images are made of distant targets over long atmospheric paths, local variations of the refractive index of the air may lead to severe optical distortions and aberrations. An extreme example of such variations is the stream of hot exhaust gases on ships. The performance of infrared and optical sensors, mounted on elevated platforms on board, is strongly reduced when targets are observed through this highly inhomogeneous medium. By means of a high precision ray-tracing model, the effects are quantitatively predicted and compared with measured data. In another application the model is used to predict distortions such as caused by atmospheric layers of variable wind speed, pressure and temperature. In this kind of atmospheric conditions, aircrafts tend to make irregular motions, which can be dangerous in landing operations. The distortions provide information on the presence of this kind of dangerous conditions: the magnitude and the location of the so-called "air pockets". The installation of a suitable distortion measurement system together with an advanced meteorological station (including LIDAR) provides great opportunities to act as a warning device in the neighbourhood of airports. Sample calculations are presented as illustration of the prediction method.

Keywords: atmospheric propagation, refraction, optical distortion, sensor performance

1. INTRODUCTION

For astronomers it is well known that the perception of stars is greatly reduced and limited by atmospheric turbulence [1]. Rapid and local small-scale changes in the refractive index cause serious deformations of the wave-front from point targets at long distance. Modern techniques have been developed to measure the wave-front deviations [2] and to apply correcting adaptive optical systems [3]. It is well known [1], that the atmospheric turbulence close to the receiving optical system has a greater impact on its resolution than the turbulence at other parts of the light path. This phenomenon leads to the conclusion that one has to be careful when selecting a place for a sensor package on board of a platform (vehicle, aircraft, helicopter, ship). Hot exhaust gases, moving to the Line of Sight (LOS), already interfering by their contributions to the radiance level in IR sensors, can in addition seriously degrade the spatial resolution. As a result the recognition range for extended targets and the detection range for point targets will be reduced. Hot exhaust plumes do on the other hand also influence the detection performance for sensors from the other direction, such as seekers homing on the hot exhaust. A special case is the performance reduction of a laser system looking through a plume and being blurred twice, one time in the outgoing beam and one time in the returning beam. Figure 1 shows a simulated example of optical blurring by local turbulence at various places of a 3m path between source and receiver. The pictures show clearly that the presence of the blurring screen (sheet of bubbled polythene) close to the receiver has a dramatic effect on the resolution, especially for the visual camera system. The wave-front distortions are negligible for the IR camera.

In this paper we pay attention on the hot exhaust gases such as ejected by gas turbine engines on board of ships. In this example, not only the amount of gases is impressive, but also their speed and high temperature, moderated by the speed of the ship. The sensor systems concern Infrared Search and Track [4] and surveillance systems [5]. Atmospheric effects do generally limit the range performance of this kind of sensors. [6-8]. The investigation of the blurring effect by the hot gases has been done by means of the precision ray-tracing model, described before [8,9]. The strength of this model is its capability to incorporate variations of the temperature and pressure gradients along the path. These variations are known to exist. The model also allows close inspection of the behaviour of the curvature of the ray along its trajectory and of the deviations of the flatness of the wave-front at any position with sufficient accuracy. Arrival heights can be calculated with an accuracy of better than 1 cm at 20 km, which allows the analysis of intensity gain by refraction.

Optics in Atmospheric Propagation and Adaptive Systems VII,
edited by John D. Gonglewski, Karin Stein, Proceedings of SPIE Vol. 5572
(SPIE, Bellingham, WA, 2004) · 0277-786X/04/$15 · doi: 10.1117/12.565690

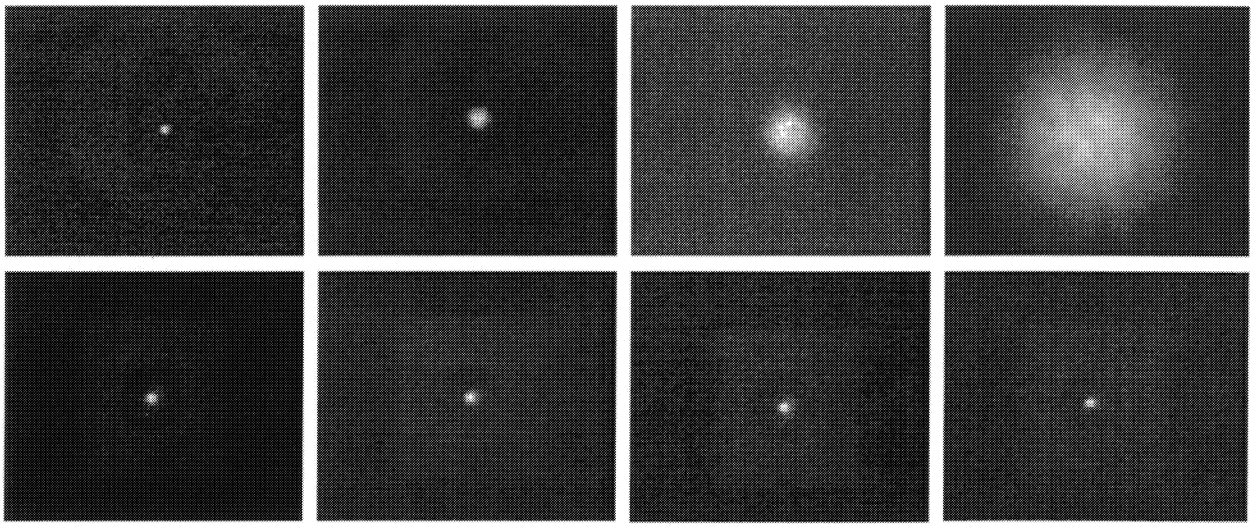

Figure 1. Illustration of optical blur by simutated local turbulence at various places between source and receiver; upper pictures: visual camera; lower pictures: IR camera (10 μm). Left: no screen; second, third and fourth column: screen 10, 30 and 100 cm from the source. Picture sizes: 19x16 mrad (above) and 51x41 mrad (below)

The ray-tracing model allows also detailed studies of atmospheric distortion by larger scale density (and thus refractive index) fluctuations along the path. This kind of fluctuations may be local temperature or pressure increases or decreases, or may be a consequence of wind-shear effects. All of them can be felt by in-flight passengers and may cause problems in the landing procedure. Several accidents did happen for this reason. General meteorological stations, including ground based radar, LIDAR, radiometers, scintillometers and Clear Air Turbulence (CAT) sensors, do not provide all adequate information on the presence of larger scale "air pockets", causing loss in lift. For this reason the new ray-tracing model has been used to investigate the possibility to use precision absolute distortion measurements for the prediction of the presence and the location of air pockets and their "intensity". The results are described in the second part of this paper.

2. THE MODEL

Precision calculations of ray trajectories through inhomogeneous media require a model with great flexibility. Most of the models have been developed for fast computations and assume a layered atmospheric structure, allowing large steps from one layer to the next [10]. However in the presence of a small-scale locally structured refractive index pattern, it is not allowed to take large steps and the application of Snell's law fails. It was therefore decided to introduce a model where the steps can be made as small as necessary and being oriented in about horizontal direction. For each step the ray curvature K_C is calculated, being the inverse of the radius of curvature R_c. K_C can be found from the well-known relationship [11]: $K_C = (dn/dh)/n$, where n and dn/dh are respectively the refractive index and the derivative of the refractive index with height h at a mid-path location of the j^{th} step. In Figure 2 a drawing is presented showing the principle of the ray-tracing scheme for the case of a flat earth. The formulae are somewhat simpler for a flat earth than in the original case of the curved earth surface, as described in [8]. During the j^{th} step the ray runs from point **O** to point **P** at heights h_j respectively h_{j+1} above the earth surface. At point **O** the ray makes an angle u_j and at **P** an angle u_{j+1} with the horizontal direction. The centre of curvature of the ray is M. During the $j+1^{th}$ step this centre of curvature will generally be located somewhere else, depending on the behaviour of n and dn/dh at this new step. For each step the same displacement in horizontal direction over a distance s is taken.

The refractive index and its derivative with height are functions of the air temperature and pressure. In this paper the following simplified assumptions will be used, similar to Lehn [10]:

$$n = 1 + (b / T) * 786 * 10^{-9} \qquad \text{and} \qquad dn/dh = - (dT/dh + 0.0348) * 786 * 10^{-9} * b / T^2 \qquad (1)$$

In these formulae b and T stand for barometric pressure (N/m²) and absolute temperature (K). The numerical value of 0.0348 between brackets, obtained from the derivative of the pressure with height, can be neglected when small-scale variations are considered. In taking this simplification and for a barometric pressure of 10^5 N/m² and an air temperature of 290 K, equations (1) simplify as follows:

$$n = 1.000271 \quad \text{and} \quad dn/dh = -9.35 * 10^{-7} * (dT/dh) \quad (\text{in } m^{-1}) \qquad (2)$$

The temperature dependence of the refractive index follows directly from formula (2): $dn/dT = -9.35 * 10^{-7}$ (in K^{-1}). This value means that the optical path difference of two rays, running over a path of 1 m through two air masses with a difference in average temperature of 1 °C and at the same pressure, is 0.935 μm, which is more than one wavelength for visual wavelengths. It is worth-wile to note that a pressure difference of 345 N/m² gives the same path difference.

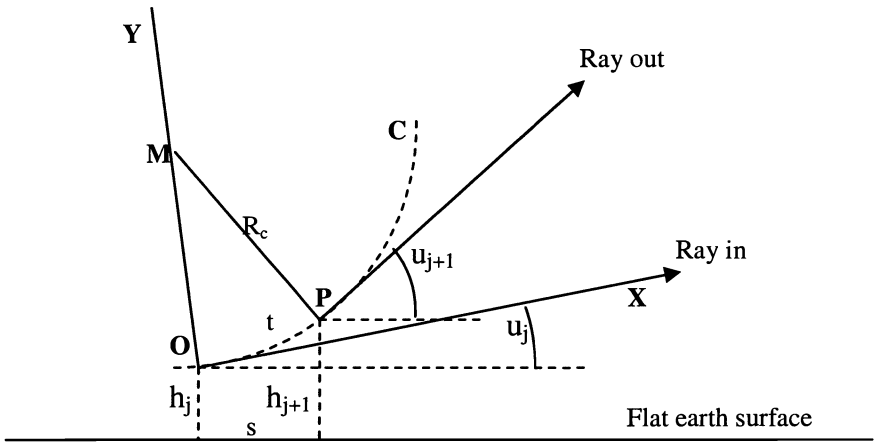

Figure 2. Geometry for the simplified flat earth ray-tracing model, illustrating the running of the ray over a path-length t from point **O** for starting the j^{th} step to point **P** for starting the $j+1^{th}$ step. The ray is curved with **M** being the centre and R_c the radius of curvature. The angles with the horizontal axis for the "Ray in" and "Ray out" of the j^{th} step are respectively u_j and u_{j+1}. One step concerns a constant horizontal displacement over the distance s.

After having calculated K_C at an estimated average height of $p = h_j + u_j/2$, the new values of h_{j+1} and u_{j+1} at point **P**, can be obtained by using the following approximations:

$$h_{j+1} = h_j + s * [\ u_j * (1 + u_j^2 / 3) + s * K_C * \{1 + u_j^2 / 2 + (u_j + K_C * s / 2)^2\} / 2] \qquad (3)$$

$$u_{j+1} = u_j + s * K_C * \{1 + u_j^2 / 2 + u_j * K_C * s / 2 + (s * K_C)^2 / 6\} \qquad (4)$$

The optical path-length along the ray between **O** and **P** is n * t, where n is the average refractive index between **O** and **P**. As we are interested in the phase differences across the wavefront, the path difference e = (n-1) * t is defined, for which the following approximation is found:

$$e = s * 1.000271 * \{ -9.35 * 10\text{-}7 * T(h) + u_j^2 / 2 + u_j * K_C * s / 2 + (s * K_C)^2 / 6\} \qquad (5)$$

in which T(h) is the temperature difference in K with T, taken at the average height p. When the path difference compared to a reference sphere is considered, the term $u_j^2 / 2$ in equation (5) has to be omitted. The path difference e is just the value for the j^{th} step. The programme, for the moment written in Quickbasic language, allows the summation of all the differences over the complete path of interest. In this manner, the rays can be followed along the path, while information on the trajectory and values of K_C and e can be shown. In the receiver plane, the arrival heights and the angles of arrival are presented. The temperature profile T(h) can be adapted at each step along the path. In this way path inhomogeneities can be incorporated. In addition tilting effects of the profiles by surface waves can be included. The ray tracing is stopped as soon as the rays hit the earth surface.

3. SOME EXAMPLES

In this section some simple examples are presented to give the reader a good feeling for the magnitude of the effects, the values K_C and e can obtain, and for the way how the temperature profile can lead to focussing effects. It will is assumed that the profiles only extend in the vertical direction. The first profile, corresponding to a kind of air bubble, located at mid-path between source and receiver, is specified as follows:

$$T_j = T(0) + T(1) * \exp [- \{(s_j - j_1 * s) / bp\}^2] * \exp [- \{(p - hpc) / hp\}^2] \quad (6)$$

Where bp and hp concern the width and the height of the bubble and j_1 and hpc its location along the path and in the vertical direction. T_j is the absolute temperature at step j; T(1) is the maximum temperature difference in the centre of the bubble with the ambient and $s_j = j * s$, the total horizontal displacement after step j. In Figure 3 the behaviour of the curvature K_C and the path difference e are shown.

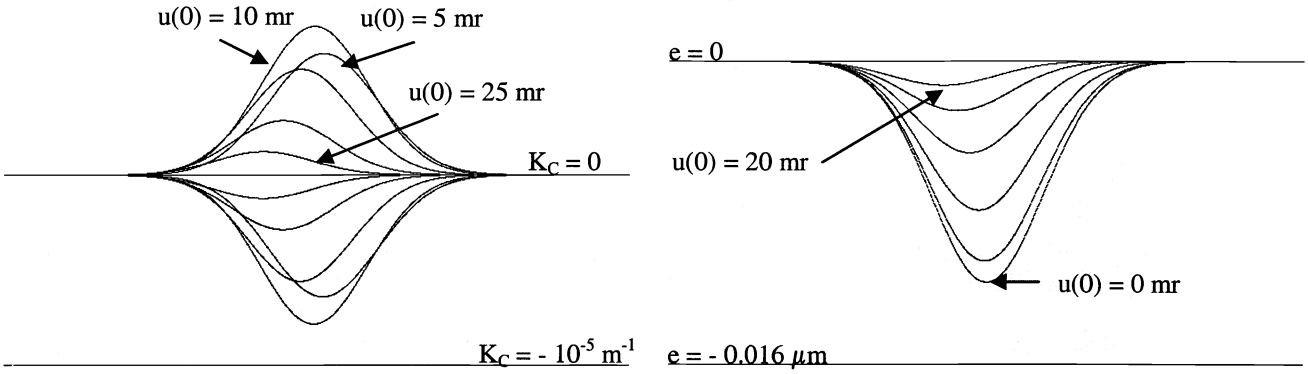

Figure 3. Curvature K_C and path difference e along the path for the case of a simplified mid-path temperature bubble

In this typical example the following assumptions have been made: source height and hpc = 20 m; hp = 0.1 m; bp = 2 m; T(0) = 290 K; T(1) = 1 K; s = 0.0125 m; j_1 = 640. The total path length, given along the horizontal axis, is 16 m for a number of 1280 steps. Plots are shown for a number of rays, leaving the point source for values of + 25 to – 25 mr for the case of K_C and + 20 to – 20 mr for the case of e. The K_C plots show curvatures up to a maximum value of about 10^{-5} m^{-1}, which corresponds to a radius of curvature of about 100 km. The maximum path difference per step is approximately 0.01 μm, which value is close to the expectation, based upon formula (2).

The second example concerns atmospheric focussing for an air bubble with lower temperature than the ambient. Again the flat earth approximation is used and the pressure gradient is omitted. A path length of 12.8 km has been chosen and the step size s is 10 m. In this case the temperature profile is specified as:

$$T_j = T(0) + T(1) * \exp [- \{(s_j - j_1 * s) / bp\}^2] * [1 / \{1 + a * (p - hpc)^2 \}] \quad (7)$$

For the different parameters the following values have been taken: source height and hpc = 20 m; bp = 1500 m; j_1 = 640; T(0) = 290 °K; T(1) = -5 °C; a = 0.03 m^{-2}. A set of 41 rays have been launched from the point source with starting angles u running from + 20 to –20 mrad with a step size of 0.1 mrad. The result of this ray-tracing example is shown in Figure 4. The flat cool air bubble with a length of 1500 m and a height of about 11 m apparently focuses the rays as soon as they are launched between + 10 and – 10 mrad. The focus is not located in one sharp point, but is horizontally stretched along the path at a height of 20 m. The program provides thus a tool for investigation of the effect of temperature and pressure profiles and their location along the path. This can be done by variation of the parameters bp, a, j_1 and hpc. Of course similar results appear, when the earth curvature and the pressure gradient is taken into account. In this case the ray-tracing plot would not be symmetric like in Figure 4.

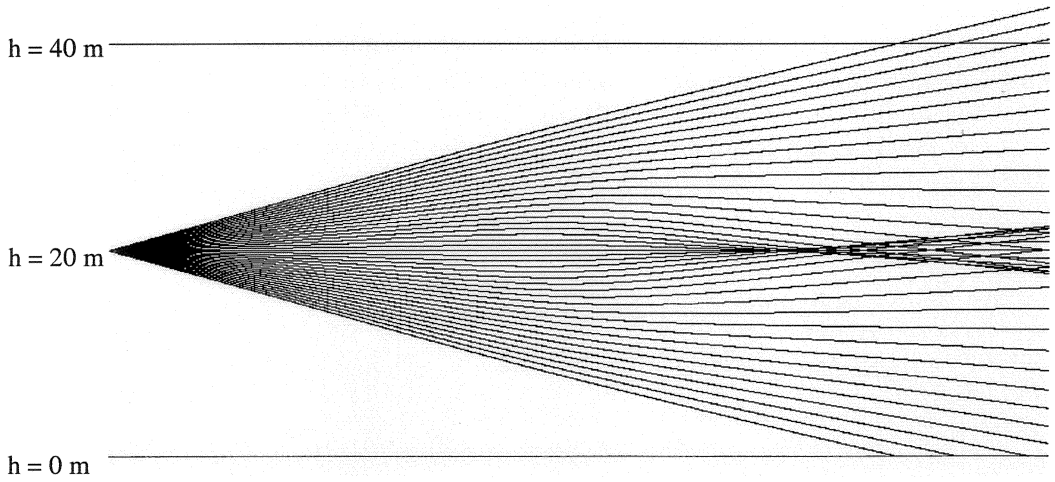

Figure 4. Example of ray tracing through a focusing atmosphere in the case of a flat earth and cool air bubble.

4. HOT EXHAUST PLUMES

The problem, referred to in this section, concerns the blurring of point targets for sensors looking through hot exhaust gases and their wake of hot air behind them. This phenomenon is of particular interest with respect to the positioning of optical and IR sensors on board of ships. In Figure 5, this type of blurring effect for ships is illustrated while a hot plume from the exhaust intervenes the line of sight between a long distance target (>15 km) and a sensor. The plume, located at a distance of about 1 km from the sensor, apparently smeared the radiance from the target over many pixels, even when the line of sight was more than 50 m behind the stack. The inhomogeneities in the plume are apparently of a larger scale than those, shown in Figure 1 and include components bigger than the pupil of the camera. The blurring is in this case similar for visible and infrared wavelengths. The severe blurring can simply be understood when one realizes that the exhaust gases are rather hot (400 °C) when leaving the stack and that the amount of gases, coming with high speed in the air per unit of time, is tremendous. They are mixed with ambient air and the mixture streams backward over the ship in nearly horizontal direction. This hot mixture tends to heat all fixed installations (eg antennas) that come on their way.

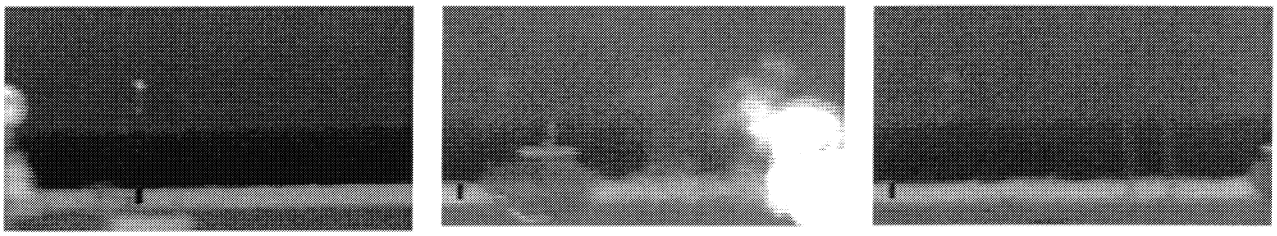

Figure 5. Illustration of blurring of a point target by hot exhaust gases fro a ship stack. The pictures were taken in day-time with Amber HS 3-5 μm camera with 250 mm lens in Den Helder (NL) 27 February 2003. Left: no intervening plume; middle: line of sight 10 m left of the stack; right: line of sight 40 m behind the stack.

In our simulation we assume that the plume consists of an array of hot air bubbles, as shown in Figure 6. For simplicity the bubbles are in this case taken two-dimensionally. For the temperature distributions in the plume the following equations have been used:

$$T_j = T(0) + 0.5 * \exp[- \{(h - hpc) / hp\}^2] * T(pl) * [1 + c * \cos \{2\pi * (h - hpc) / tpv\}] \quad (8)$$

$$T(pl) = 0.5 * T(q) * \exp[- \{(j - j_1)*s / bp\}^2] * [1 + c * \cos \{(2\pi * j * s / tph)\}] \quad (9)$$

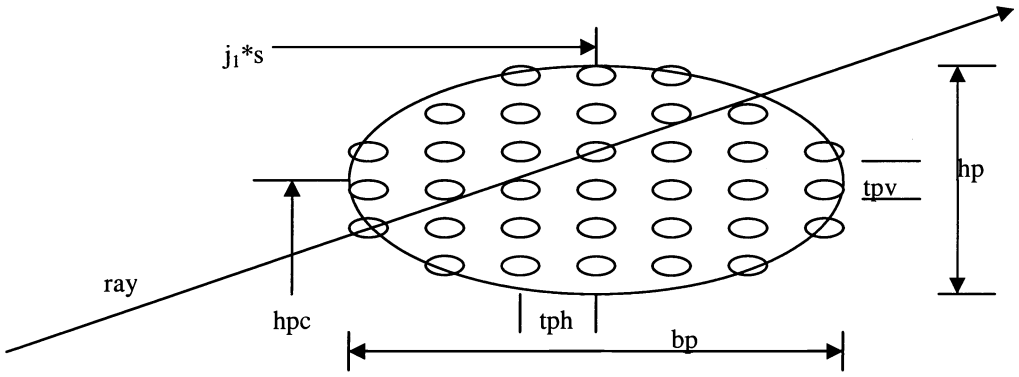

Figure 6. Modelling of the ships plume, consisting of a number of hot air bubbles, with passing light ray.

in which bp and hp determine the horizontal and vertical dimension of the plume, tph and tpv the size of the bubbles and hpc the height of the center of the plume. T(0) is again the ambient temperature (in K) for which we take again 290 K. T(q) is the average maximum plume temperature in C. The variable parameter c is chosen between 0 and 1. The derivatives of Tj versus height are becoming rather complex. For simplicity they are not presented in this paper. As the light path is becoming longer in this case, we will give the two recurrent equations for h_{j+1} and u_{j+1}:

$$h_{j+1} = h_j + s*[\ (1+ h_j/R\ )*v/2 + u_j*(1+ h_j / R + u_j^2/3\ ) + s*(1+ h_j*2/R + u_j^2/2 + (u_j + s/2R_c\ )^2\ )/\ 2R_c] \quad (10)$$

$$u_{j+1} = u_j + v + s*[1 + h_j / R + u_j^2 / 2 + v * u_j + (v + u_j) * s / 2Rc + (s / R_c)^2 / 6] / R_c \quad (11)$$

where R is the radius of the earth. If M_e is the center of the earth, v is the angle between OM_e and PM_e. An example of a ray-tracing through the plume is shown in Figure 7. The height of the point source and the center of the plume hpc are both 20 m. The size of the individual bubbles tph and tpv is 1m. The height of the plume hp and the width of the plume bp is respectively 10 m and 25 m. Furthermore we take: c = 1, T(q) = 50 C and j_1 = 800. The step size s has to be taken at least 4 times smaller than the size of the bubble in order to avoid too rapid changes of the ray-curvature when passing the bubbles. So for s we take 0.25 m and for the total number of steps 2560, which brings the total path length to 640 m. The center of the plume is located at a distance of 200 m from the source. The departure angles of the 40 rays vary from +10 to –10 mrad, with a step size of 0.5 mrad. Figure 7 clearly shows the effect of the local hot air bubbles in the plume by means of a number of focusing areas at an intermediate distance of about 400 m from the source.

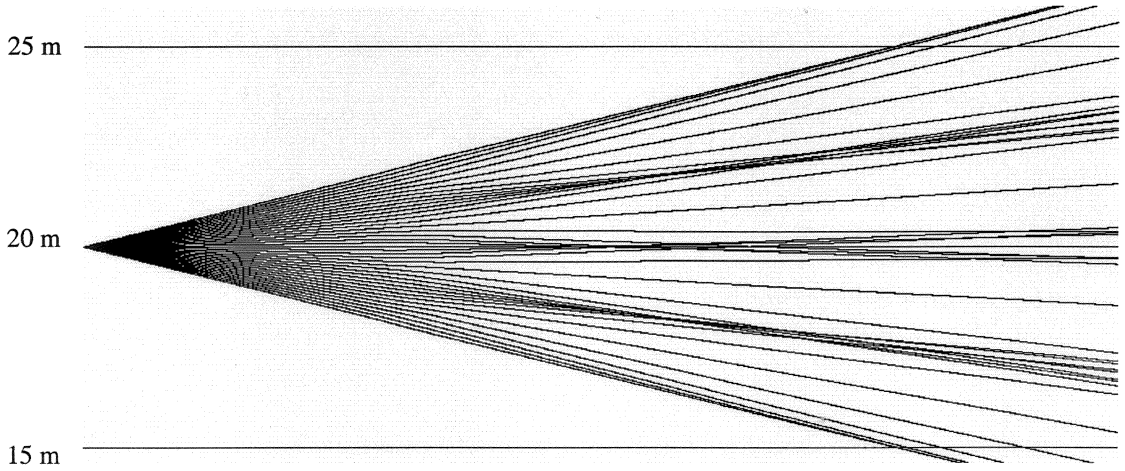

Figure 7. Example of ray-tracing through simulated plume with regularly distributed hot air bubbles.

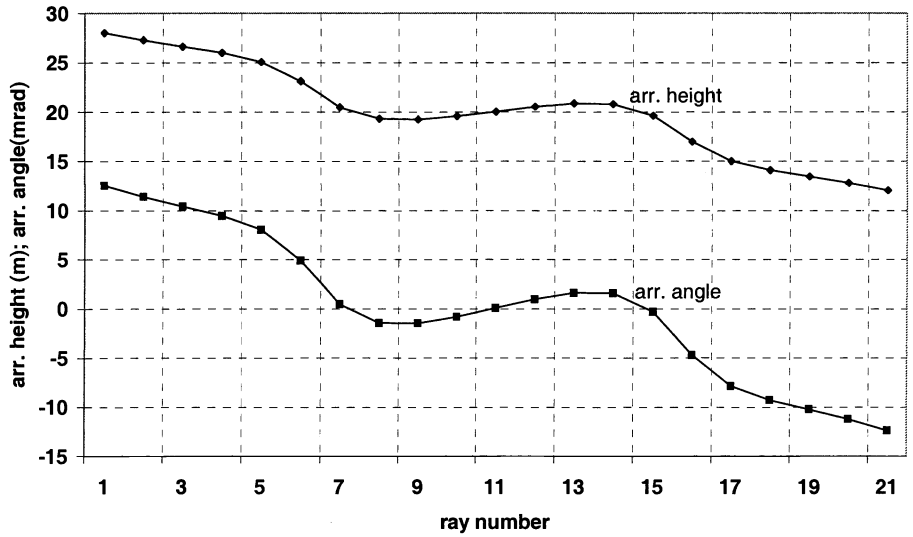

Figure 8. Arrival height and angle of arrival versus ray number (departure angle) for the case that the plume is located at a distance of 40 m from the source.

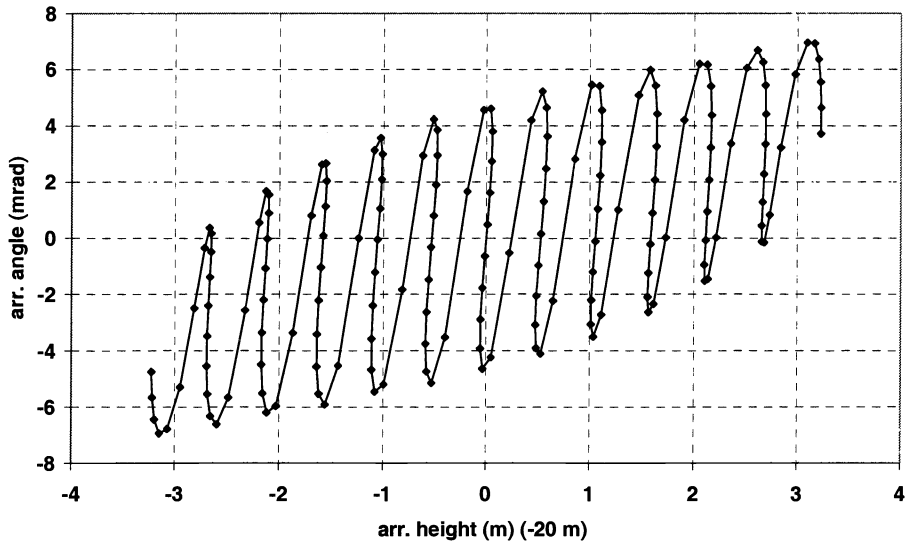

Figure 9. Angle of arrival versus arrival height, while the plume is located at a distance of 40 m from the receiver.

Figures 8 and 9 show examples of model output for the cases that the plume is located close to the source and close to the receiver. In these cases the plume is characterized by the parameters: hp = 10 m, bp = 25 m, tph = 2 m, tpv = 0.5 m and T(q) = 50 C. The step size s = 0.125 m and the total number of steps is 5120, providing a path length of 640 m. For j_1 we have chosen 320 (Figure 8) and 4800 (Figure 9) and a total number of 160 rays were sent through the plume with departure angles between –100 and +100 mr (Figure 8) and –20 and +20 mr (Figure 9). The plots show clearly the difference in blurring effect in both cases. In the case of the plume close to the source, the maximum blur is about +/- 0.5 mr (1 mr total) for the center of the arrival height and for a 10 cm pupil. For the case of the plume near to the receiver, the angles of arrival vary considerably for nearly the whole area in the "shadow" of the plume, which leads to a blurring of +/- 4 mr (8 mr total). The latter case is giving a very similar blurring effect as the measured blurring, shown in Figure 5. The model apparently provides a suitable tool for simulation of distortion by hot exhaust plumes.

5. DISTORTION BY AIR POCKETS

Following the success of previous distortion measurements and the associated modeling described in [8], an investigation has been undertaken to find out if it feasible to measure the presence of "air pockets", areas of drastic local changes in density and thus refractive index by means of a high resolution camera system. The scenario for such a set-up is illustrated in Figure 10, where a set of sources and receivers (cameras) is installed in two planes **A** and **B**, perpendicular to the earth surface. In the range between A and B, there may be a local deviation of the air density (eg the temperature - or pressure gradient). The cameras are characterized by high geometrical resolution, as allowed by the atmospheric blur, and a built-in precision absolute horizon indication. This knowledge of this horizon position allows the measurement of tiny ray deviations by refraction. One camera could for example consist of a relatively cheap diffraction limited telescope with 1 m focal length, a pupil size of 0.1 m and a CCD array with 6 μm pixels, giving a spatial resolution of 6 μrad. Most of the time the atmospheric blur for ranges of more than 10 km is more than this value. The use of multiple sources and cameras allow a kind of stereoscopic view through the air mass between A and B. By careful analysis of the absolute positions (above the geometrical horizon) of each of the sources in the field of view of each of the cameras, one should be able to determine the presence, the location and the intensity of the air pocket.

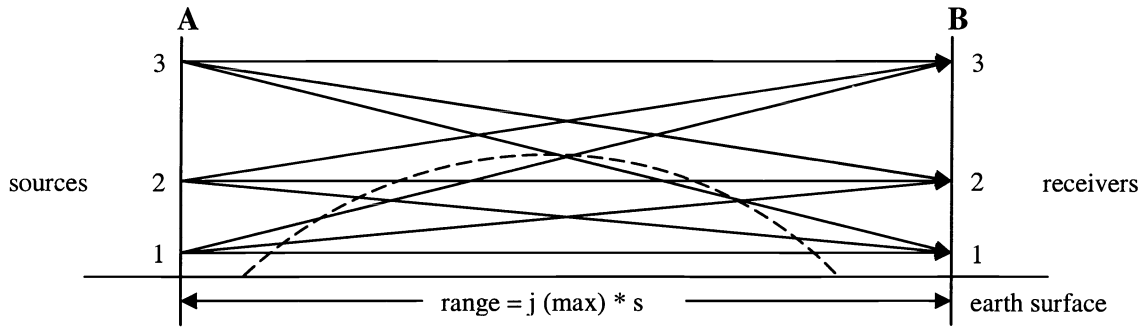

Figure 10. Illustration of the scenario for detection of a possible local inhomogeneity in the vertical density gradient, indicated in the figure by the dashed arc. The total number of steps along the path is j (max)

In our example the following variation of temperature and its derivative with height has been taken:

$$T = T(0) + (z / a) * \{\exp(-a * h) - 1\} - 0.006 * h \quad \text{and} \quad dT/dh = -z * \exp(-a * h) - 0.006 \qquad (12)$$

In these equations the term –0.006 * h is coming from the well known adiabatic temperature drop with height. The value of (z / a) has the meaning of the temperature difference at infinite height and at height zero, when neglecting the adiabatic term. The parameter a is responsible for the steepness of the temperature decrease/increase with height. When (z / a) is positive, the temperature decreases with height, resulting in a sub-refractive condition: the rays tend to bend upward.

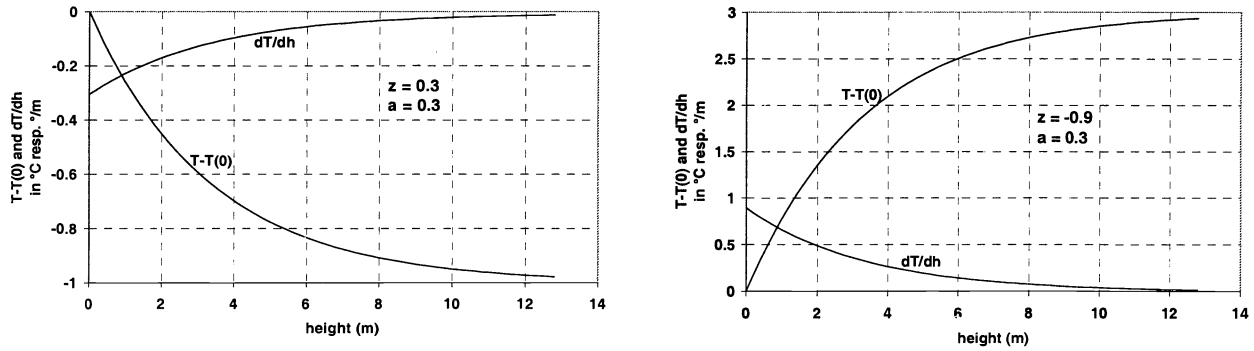

Figure 11. Plots of T-T(0) and dT/dh versus height for two different combinations of the parameters z and a

An impression of the behaviour of the functions T and dT/dh according to equations (12) can be obtained from the plots in Figure 11, where two combinations of the parameters z and a have been taken. In our example we have taken the values z = 0.3 °/m and a = 0.3 m^{-1} for the two ends of the path. At the intermediate steps the parameter z is changing per step according to the relationship:

$$z_j = z_0 - z_m * \exp - \{(j - j_m) * s / s_m\}^2 \qquad (13)$$

in which z_j is the value of z at step j, z_0 the value of z at the beginning of the path, j_m the step where the parameter z_j reaches its maximum value, z_m the value of z at this maximum and s_m the width of the temperature deviation. In our case we have taken the following values for these parameters: z_0 = 0.3 °/m, s = 10 m, s_m = 640 m, j_m = 320, 640 and 960, while the total number of steps was 1280, resulting in a total path length of 12.8 km. For z_m we have taken a number of values, ranging from 0 to 2.4 °/m. This latter value corresponds to a maximum temperature rise of +7 C in the center of the deviation.

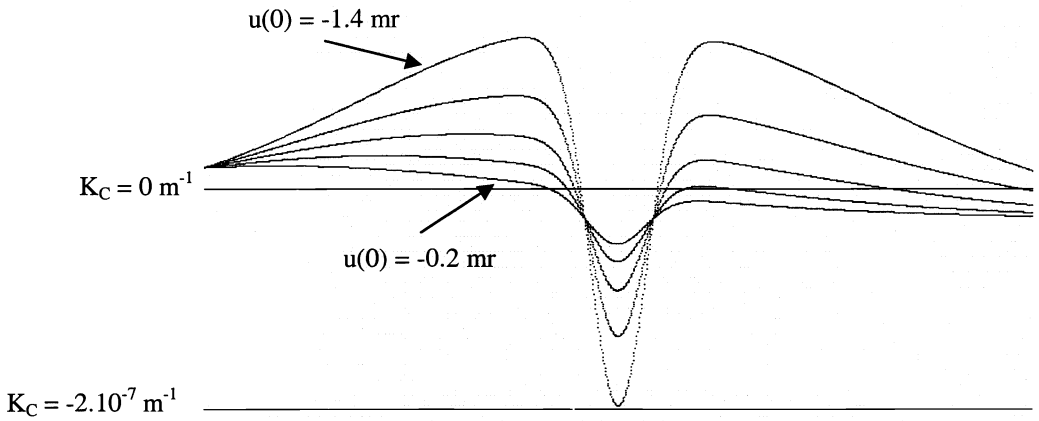

Figure 12. Variation of K_C along the path of 12.8 km with a mid-path, local temperature inhomogeneity. The departure angles for the five rays were: - 0.2 mrad, - 0.5 mrad, - 0.8 mrad, - 1.1 mrad and - 1.4 mrad. The source height was 6 m.

It is interesting to follow the behaviour of the curvature along the path in this example. Figure 12 shows a typical example for the case of z_m = 0.6 °/m at the location: j_m = 640 (mid-path). The value of z_m corresponds to temperature difference of about +2 °C at 10 m height and at zero level. The rays start with a positive curvature (bending upward), then near mid-path the curvature becomes negative (rays bending downward) and then after the air pocket, the rays turn back to upward bending. The most negative curvature becomes – 2.10^{-7} m^{-1}, equivalent to a radius of curvature of about 5000 km.

Instead of putting the source at a height of 6 m we can put a camera at this height and see under what absolute angles an array of sources is perceived, mounted at the heights: 8, 9, 10, 11, 12, 13 and 14 m. If there would be no atmospheric refraction, these sources would be observed at angles: 641, 563, 485, 407, 328, 251 and 173 μrad below the horizon. For the conditions given before with the slightly sub-refractive atmosphere and without air pocket (z_m = 0), these perception angles become: 1497, 1191, 1007, 858, 727, 608 and 497 μrad. The refraction effect is very clear by comparison of these two arrays of angles. By introducing the air pocket in the light path, the source observation angles are further influenced. Figures 13 shows quantitatively plots of these angles for the different source heights, where the deviation with respect to the free space observation angle is given. The angles, being the down-look angles, are quite different for the three locations of the air pocket and for the five different values of z_m. It is required in this case that one is able to measure the absolute observation angle. It is also possible to measure the observation angles between the sources. Predictions are shown in Figure 14, again for the seven sources, three pocket locations and five values of z_m.

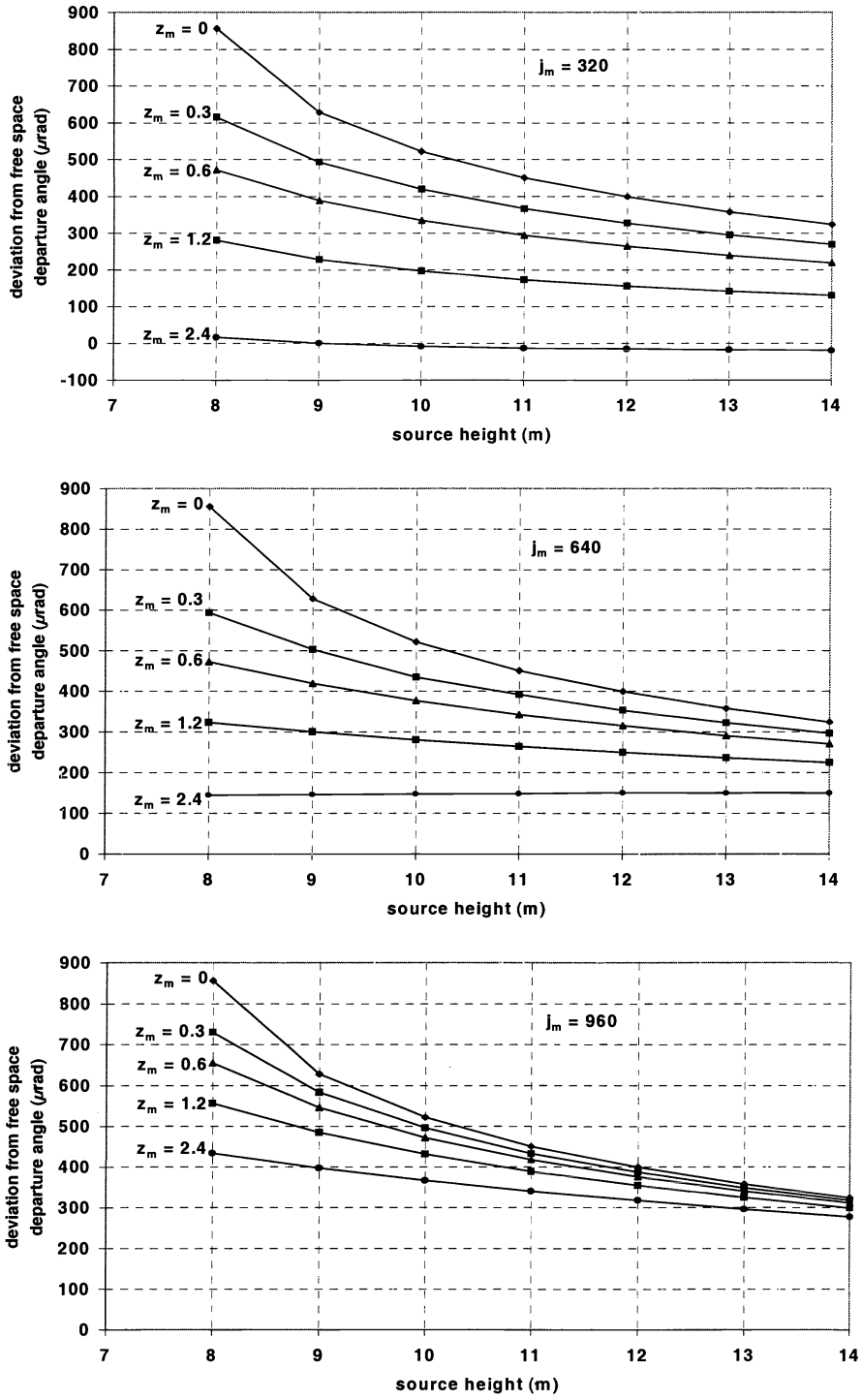

Figure 13. Angular deviations of observation angles with free space observation of seven sources for three locations of an air pocket: $j_m = 320$ (near camera) $j_m = 640$ (mid-path) and $j_m = 960$ (near sources)

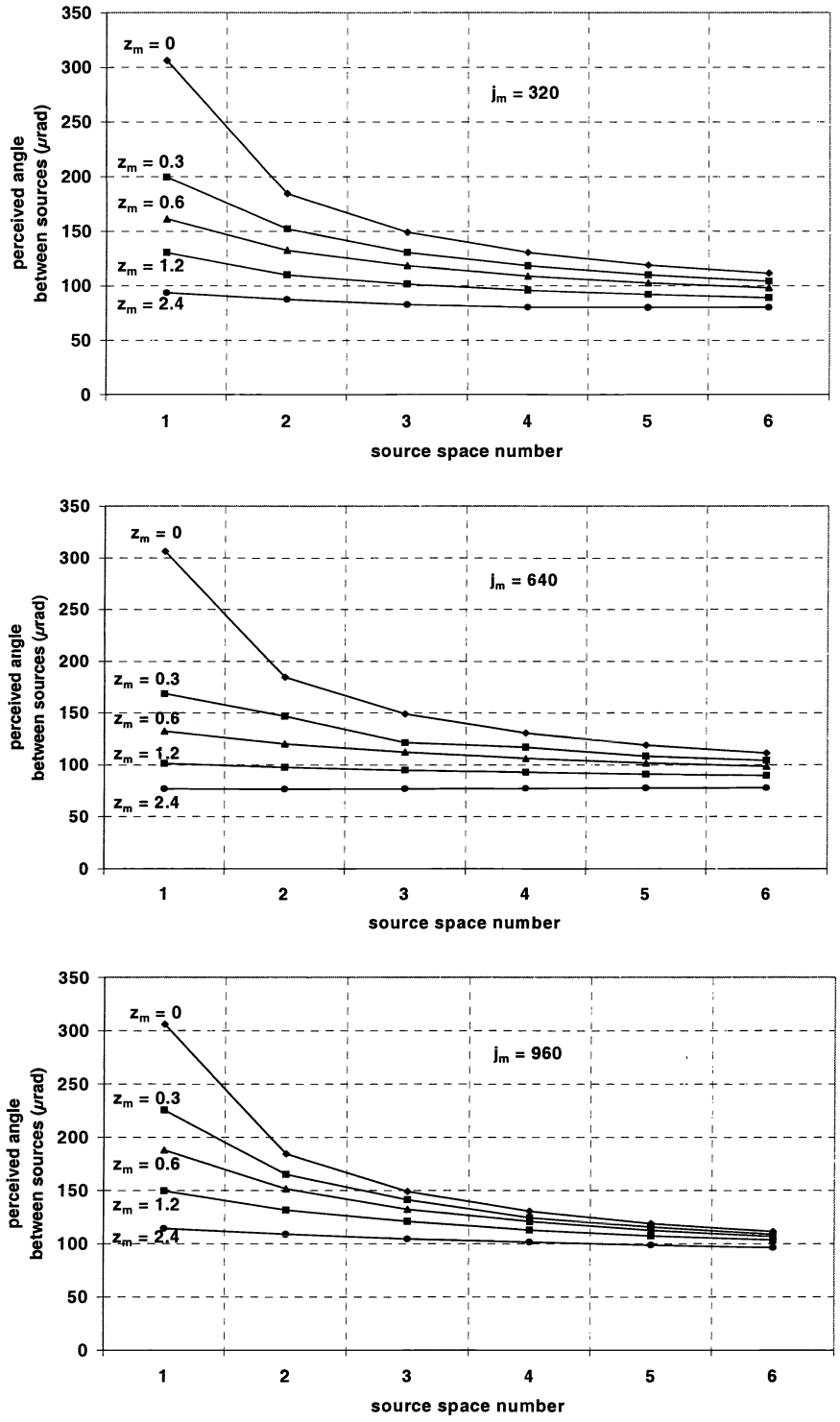

Figure 14. Differences in perceived angles between sources for three pocket locations and five values of z_m

The non-linearity of the plots of Figure 14 show the distortion by atmospheric refraction. It is noted, that the actual angle between each of the sources should be 78 μrad. In most cases, this angle is larger due to the sub-refractive nature of the atmosphere without air pocket. The non-linearity decreases with increasing strength of the air pocket, i.e. for larger z_m value. The angular separation is the biggest for the lower sources (source space number 1 between the source at 8 m and the source at 9 m. The angular separation between the sources at 13 and 14 m is becoming more closely for all cases. Keeping in mind the angular resolution of the camera (6 μrad), it is clear that this resolution is enough to establish the presence, location and strength of an air pocket by measuring both the absolute observation angles (Figure 13) and the relative angles between the sources (Figure 14). It is recommended to use carefully measured air temperature data at both sides of the line of sight at various heights, in order to be used as input parameters for a simultaneously operated ray-tracing model, predicting the atmospheric distortion by refraction.

6. CONCLUSIONS

In this paper the use of a precision ray-tracing model has been presented for two practical applications: blurring by hot exhaust gases and precision distortion measurement for the detection of air pockets. The effect of the presence of an inhomogeneous hot air plume on the variation of the angle of arrival of rays emitted by a point target at long distance and arriving at a sensor pupil, has been investigated quantitatively and compared with measured data. The importance of the location of the plume compared to the position of the sensor and the source has been illustrated. The flexibility of the model, applied to non-homogeneous atmospheric conditions along the path, was demonstrated.

In the second application, a set-up has been described for precision angular measurement of apparent positions of point sources, observed over a path of 12.8 km. The application is the investigation of the feasibility of such a system for the detection of atmospheric layers with strongly deviating air density (temperature, pressure), which may lead to dangerous situations for aircraft in their landing procedure. This layer (or bubble or air pocket) tends to have strong variation of the refractive index with height. The simulation shows that the observation system, realized with affordable components, is well capable to detect the presence, location and the strength of the air pocket by measuring the absolute and relative angles for an array of sources. If one camera does not provide all required information, it may be worth-wile to install a second one in order to get more precision on the location of the air pocket.

REFERENCES

[1] Marcel G.J. Minnaert, *Light and Color in the outdoors*, Springer Verlag, New York, 1993. p. 92
[2] Joseph M. Geary, *Introduction to Wavefront Sensors*, SPIE Tutorial Text TT18, Bellingham, 1995
[3] Robert K. Tyson, *Introduction to Adaptive Optics*, SPIE Tutorial Text TT41, Bellingham, 2000
[4] Arie N. de Jong et al, *IR panoramic alerting sensor concepts and applications*, SPIE Volume 5074, Infrared Technology and Applications XXIX, Orlando, April 2003
[5] A.N. de Jong et al, *IR detection of small invading surface targets in littoral waters*, Proceedings 5th MSS symposium, Gaithersburg, December 2002
[6] Arie N. de Jong et al, *Enhanced IR point target detection by atmospheric effects*, SPIE Volume 4820, Infrared Technology and Applications XXVIII, Seattle, July 2002
[7] Arie N. de Jong, *Intensity variations of small airborne incoming targets, popping-up above the horizon*, SPIE Vol. 5237, International Symposium on Remote Sensing, Barcelona, September 2003
[8] Arie N. de Jong, *Refraction effects of atmospheric inhomogeneities along the path*, SPIE Vol. 5237, International Symposium on Remote Sensing, Barcelona, September 2003
[9] Arie N. de Jong et al, *Atmospheric refraction effects on optical/IR sensor performance in a littoral-maritime environment*, 2nd version of paper submitted to Applied Optics, March 2004
[10] Waldemar H. Lehn, *A simple parabolic model for the optics of the atmospheric surface layer*, Appl. Math. Modelling, Vol. 9, December 1985
[11] Max Born and Emil Wolf, *Principles of Optics*, 7th ed. Cambridge University, Cambridge UK, 1999, p. 122